Study of gas-puff Z-pinches on COBRA

N. Qi,[1,a)] E. W. Rosenberg,[1,b)] P. A. Gourdain,[1,c)] P. W. L. de Grouchy,[1] B. R. Kusse,[1] D. A. Hammer,[1] K. S. Bell,[1,d)] T. A. Shelkovenko,[1] W. M. Potter,[1] L. Atoyan,[1] A. D. Cahill,[1] M. Evans,[1,b)] J. B. Greenly,[1] C. L. Hoyt,[1] S. A. Pikuz,[1] P. C. Schrafel,[1] E. Kroupp,[2] A. Fisher,[2] and Y. Maron[2]
[1]*Laboratory of Plasma Studies, Cornell University, Ithaca, New York 14853, USA*
[2]*Weizmann Institute of Science, Rehovot 76100, Israel*

(Received 13 June 2014; accepted 18 September 2014; published online 6 November 2014)

Gas-puff Z-pinch experiments were conducted on the 1 MA, 200 ns pulse duration Cornell Beam Research Accelerator (COBRA) pulsed power generator in order to achieve an understanding of the dynamics and instability development in the imploding and stagnating plasma. The triple-nozzle gas-puff valve, pre-ionizer, and load hardware are described. Specific diagnostics for the gas-puff experiments, including a Planar Laser Induced Fluorescence system for measuring the radial neutral density profiles along with a Laser Shearing Interferometer and Laser Wavefront Analyzer for electron density measurements, are also described. The results of a series of experiments using two annular argon (Ar) and/or neon (Ne) gas shells (puff-on-puff) with or without an on- (or near-) axis wire are presented. For all of these experiments, plenum pressures were adjusted to hold the radial mass density profile as similar as possible. Initial implosion stability studies were performed using various combinations of the heavier (Ar) and lighter (Ne) gasses. Implosions with Ne in the outer shell and Ar in the inner were more stable than the opposite arrangement. Current waveforms can be adjusted on COBRA and it was found that the particular shape of the 200 ns current pulse affected on the duration and diameter of the stagnated pinched column and the x-ray yield. © *2014 AIP Publishing LLC*. [http://dx.doi.org/10.1063/1.4900748]

I. INTRODUCTION

High current Z-pinches driven by pulsed power machines are an excellent way to produce high energy density plasmas.[1–5] The magnetic field associated with the high current has been used to implode plasmas from cylindrical wire arrays, cylindrical liners, and coaxial gas-puff configurations. The resulting hot, dense pinched plasmas are commonly used as intense X-ray sources. Z-pinch implosion times are typically 100 ns with implosions driven by current pulses as high as tens of MA.[6,7] Z-pinches with longer implosion times (>200 ns) hold the promise of higher energy coupling efficiency, lower driver voltage, and less expensive drivers. To match Z-pinch loads to slower drivers, larger initial load radii, R_0, are needed to accelerate the imploding loads for a longer time in order to achieve the ion kinetic energy and compression ratio required to achieve a strong pinch, high temperature, and high plasma density near peak current. A major problem in producing a strong pinch is the hydromagnetic Magneto-Rayleigh-Taylor (MRT) instability. For single shell or uniform fill gas puff Z-pinch implosions, the MRT instability grows exponentially with a growth rate of $(g/\lambda)^{0.5}$, where g is the acceleration and λ is the wavelength. Assuming constant acceleration and an initial radius R, the MRT grows to an amplitude given by an exponential factor of $(R/\lambda)^{0.5}$. Large initial radius single shell Z-pinches have a much larger MRT instability growth than smaller radius loads. To mitigate the MRT instabilities, Z-pinch loads with tailored radial density profiles have been suggested.[8] Such advanced Z-pinch loads using double and/or triple gas-puffs for 200–300 ns implosion times have been tested on the 3 MA Double Eagle at L-3 Communications, the 5 MA Decade Quad at Arnold Engineering Development Center, and the 6 MA Saturn at Sandia National Laboratories. These Z-pinches with density profiles predicted to reduce the MRT instability growth actually did so and produced impressive pinch stability and/or increased X-ray radiation yields.[9–11] These results have motivated us to look in more detail at 200 ns gas-puff Z-pinch implosions with tailored density profiles.

Our gas-puff Z-pinch experiments were conducted on the 1 MA Cornell Beam Research Accelerator (COBRA) pulsed power generator at Cornell University.[12,13] COBRA has the advantage of a high pulse rate (up to five per day) and an adjustable current pulse rise-time of 100–240 ns with variable pulse shapes. A double-annular, 6 cm outside diameter gas-puff valve was used to establish the radial plasma density profiles. Implosion stability properties were investigated using various combinations of neon (Ne) and argon (Ar) in the inner and outer annular gas puff shells. The gas puff Z-pinches were also studied with an Al wire on or 3 mm off the pinch axis. It was determined that the dynamics of the implosion also depended on the waveform of the 200 ns current pulse.

An extensive set of diagnostics was employed to characterize the gas-puff Z-pinches from the initial gas phase through pre-ionization and implosion, to the final pinch

[a)]Permanent address: L-3 Applied Technologies, Inc., San Leandro, California 94577, USA.
[b)]Present address: Stanford University, Stanford, California 94305, USA.
[c)]Present address: University of Rochester, Rochester, New York 14627, USA.
[d)]Present address: Sandia National Laboratories, Albuquerque, New Mexico 87185, USA.

phase. The initial gas-puff density profiles used in the present experiments were measured with Planar Laser Induced Fluorescence[14–16] (PLIF). A multi-frame Laser Shearing Interferometer[17,18] (LSI) and a Laser Wavefront Analyzer[19] (LWA) were used to measure the plasma density profile during the implosions. Two 2-ns gated, 4-frame extreme ultraviolet (XUV) cameras captured images of the imploding plasma. Filtered pinhole cameras recorded the X-ray images during stagnation and filtered X-ray diodes provided time resolved data on the X-ray emission. Radially resolved visible light spectra from the imploding plasma were recorded to give plasma density and temperature information. The imploding plasma K-shell X-ray spectra were measured with a spatially resolving spherical crystal spectrometer.

The remainder of this paper is organized as follows: Sec. II describes the current pulses, hardware and specialized diagnostics developed for these experiments; Sec. III presents the results and discussions of the Ne/Ar Z-pinch stability studies, including the effects of the current waveform on implosion dynamics; and Sec. IV gives the conclusions and future experiments.

II. COBRA, HARDWARE, AND DIAGNOSTICS

In this section, the COBRA current pulse waveforms used for these experiments, the gas-puff hardware and the diagnostics specifically developed for the gas-puff experiments are described.

A. COBRA current pulse waveforms

For these experiments, two types of current waveforms were used, as shown in Figure 1. Both types of pulses were about 200 ns in duration with two prominent current peaks. The pulse with the solid line had the first peak smaller than the second, while the first peak was higher than the second in the pulse with the dotted line. Consequently, the second had about twice the dI/dt and voltage during the initial rise. Also notice that there was essentially no pre-pulse in either of these waveforms. This is an important feature for gas-puff experiments on COBRA and required pre-ionization of the gas-puff, as will be discussed later.

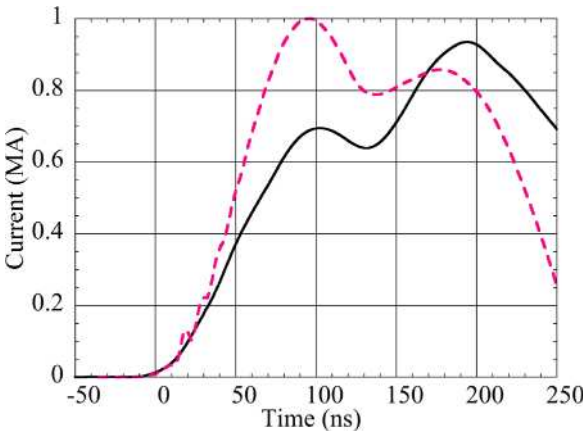

FIG. 1. Examples of the two types of the current waveforms are shown.

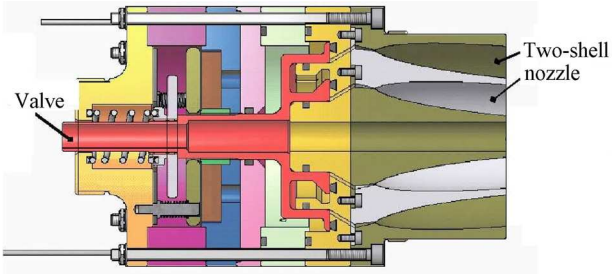

FIG. 2. Schematic drawing of the double-shell nozzle and valve. A central hole permitted diagnostic access up the axis. Future implementations of this nozzle will have a central gas jet, i.e., three concentric gas puffs.

B. Gas-puff hardware

The gas-puff valve and nozzles used for these experiments were similar to the ones reported in Ref. 20. The gas-puff valve and nozzle system were designed and fabricated by the Z-pinch plasma physics group at the Weizmann Institute of Science. Figure 2 shows a cross-sectional view of the assembled device. The outer nozzle output has a radial annulus spanning from 2 to 3 cm and the inner nozzle has an annulus from 0.7 to 1.8 cm. Both were made of aluminum (Al). Flexibility in tailoring the radial gas density profile and species was made possible by independent plena for each nozzle. In the configuration used for these experiments, the valve had a 1 cm hole down the center for axial diagnostic access, as is shown in Fig. 2.

Supersonic gas-puffs were injected from the double-nozzle (cathode) into the Z-pinch load region. An electrical breakdown signal was produced by a spark gap located in the outer gas-puff nozzle throat, providing a timing signal for the gas injection. The gas flow reached a density plateau in the load region about 500 μs after the breakdown signal.

The gas-puff valve is shown mounted in the COBRA load region in Fig. 3. The vacuum chamber surrounding the load region was 90 cm in diameter. The top of the double-nozzle gas-puff valve was flush with the cathode surface. The anode plane was formed by a 2.5 cm thick, 12 cm diameter stainless steel ring with eight 3 mm diameter stainless steel rods oriented radially towards the center. Four return

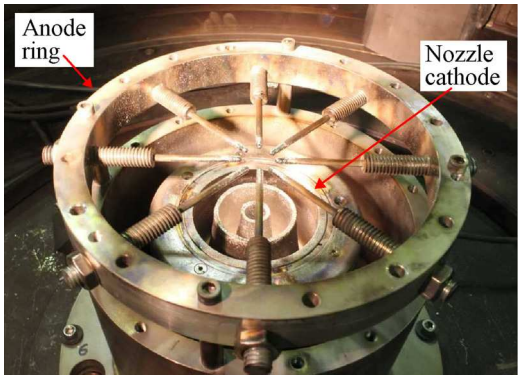

FIG. 3. Overview of the COBRA gas-puff load region. The cathode consisted of the exit plane of the two-annulus nozzle with an 8-mm diameter hole in the center. The anode was a stainless steel ring with eight 3-mm diameter radial rods and was connected to the machine anode by 4 return current posts.

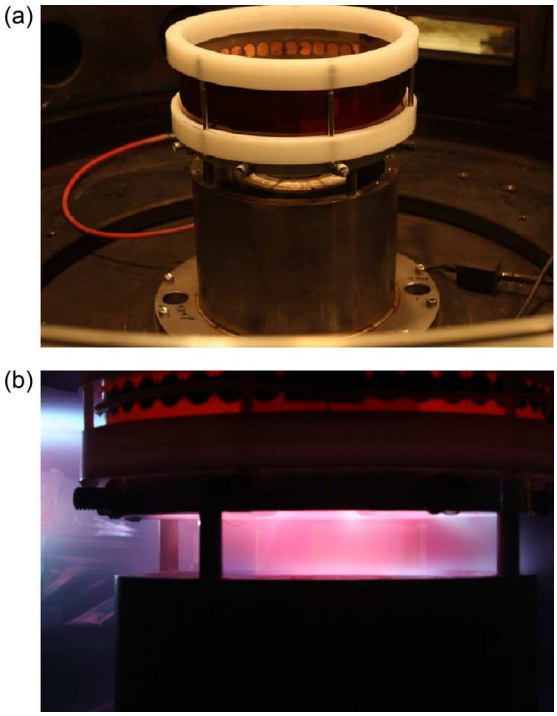

FIG. 4. (a): COBRA Z-pinch load with a flashboard UV pre-ionizer. (b): Visible emission from the Ne gas-puff when the flashboard was pulsed by a 25 kV, 5 μs power supply.

current posts below the anode ring, equally spaced on a 13 cm diameter, connected the anode plate to the ground.

Because of COBRA's small pre-pulse, as shown in Fig. 1, it was necessary to implement a gas-puff pre-ionizing system to lower the initial load impedance and reduce unacceptably high load voltages and power reflection. Initially, a 16-cm diameter flashboard pre-ionizer was placed about 4 cm above the anode as shown in Fig. 4. The lower image in Fig. 4 shows the visible light emission from a Ne gas-puff excited by the UV flashboard radiation. However, using the flashboard UV pre-ionizer, we observed that the gas-puff Z-pinch load still presented an impedance that was too high for about 40 ns. This reflected an unacceptable amount of power back toward the driver as indicated by the oscillation in the dI/dt trace (the time derivative of the implosion current, red dashed line) in Fig. 5. The UV radiation from the 25 kV, 0.3 μF, 5 μs flashboard was not intense enough to effectively photo-ionize gas. It was replaced by a 5 kV, 14 μF, 30 μs discharge source that directly injected electrons into the gas-puff. As shown in Fig. 5, the dI/dt signal (black line) with the arc plasma source was more or less the same as seen with the more standard inductive/resistive COBRA loads. There were no high amplitude oscillations in the dI/dt signal. The arc source provided a sufficient initial conducting current channel and was used in all the gas-puff Z-pinch experiments discussed in this paper.

C. Diagnostics

The diagnostics and their locations around the COBRA load region are shown in Fig. 6. The time gated XUV cameras, X-ray pinhole cameras, X-ray crystal spectrometer,

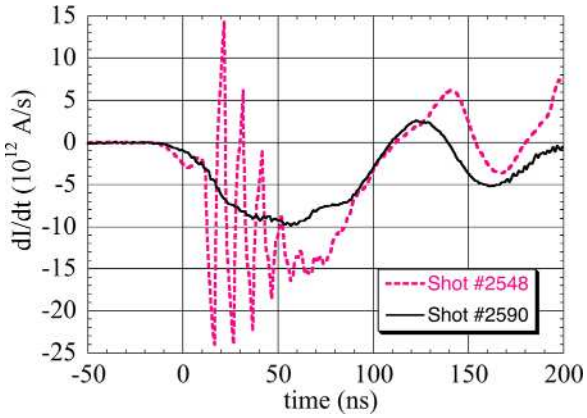

FIG. 5. The time derivative of the implosion current, dI/dt, measured by a Rogowski coil. The red dashed line is the dI/dt with the UV flashboard pre-ionizer (COBRA pulse #2548). Large amplitude oscillations 30-60 ns after the start of the current pulse indicate a high load impedance. Using an arc source to inject electrons directly into the load region, the dI/dt signal (black line, COBRA pulse #2590) looked like a typical COBRA pulses with a wire-array Z-pinch load.[21,22]

filtered Photo-Conducting Diodes (PCD's), and fiber coupled visible spectrometer are standard diagnostics on COBRA. The LWA and LSI were installed specifically for gas-puff Z-pinch experiments, in which the plasma and the diagnostic laser beam, to be described shortly, are comparable in diameter. The principles of operation of the LSI and LWA have been reported in Refs. 17 and 19. The LSI has the advantages of providing visualized plasma shape *in situ*, high spatial image resolution (50 μm or better) and relatively high sensitivity, but its fringe analysis for density determination is complicated and time consuming. The LWA gives straightforward density measurements, but with reduced spatial resolutions (several hundred μm) limited by the micro-lens size and relatively low sensitivity. Thus, the LSI is more suitable for early implosion phase, where the fringe shifts are relatively small and easy to identify, and the LWA works better for later implosion times, where the plasma refraction is large.

A PLIF system was used for determining the initial r-z neutral gas density profiles in a separate vacuum chamber.

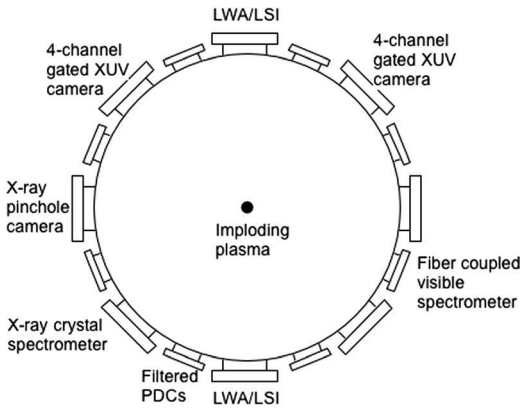

FIG. 6. Diagnostic arrangement for the gas-puff Z-pinch experiments. The three-channel LSI/LWA viewed the imploding plasma with about 3° between beams and the two 4 channel EUV cameras were 90° apart.

1. Laser wavefront analyzer

The principles of operation of the LWA for Z-pinch density measurements have been reported in Ref. 19. In our LWA, the 100-ps, ~30-mJ/pulse, 532-nm, ~50-mm diameter Nd:YAG laser beam passed through and was refracted by the gas-puff plasma. This refracted beam was then passed through a 2-D array of micro-lenses to form many small beamlets that were focused on the detector of a CCD camera. In the absence of plasma refraction, the beamlets form a set of uniformly spaced dots. The density gradients in the plasma refract the laser beam and cause the position of the dots to shift. From this shift, the plasma density profile can be obtained. Figure 7 depicts the operation of this diagnostic.

2. Small shift laser shearing interferometer

The operation of the small shift LSI is described in Ref. 17. Unlike a Mach-Zehnder interferometer, in which the interference pattern directly yields the phase shift of the laser beam after passing through the plasma, the small shift LSI image represents the spatial derivative of the phase front with respect to the shearing direction. This is actually an advantage for the Abel inversion because it is the derivative of the phase front that is needed for the Abel inversion integral. For this to be the case, the shift must be relatively small over the density variation length scale of the plasma.

Figure 8 depicts the operation of our LSI. Notice that the small shift LSI data shows interference fringes over essentially the entire laser beam diameter. This image was taken relatively early in time, about 60 ns before peak current in the solid line pulse in Fig. 1, where the LWA signal to noise ratio is too low to obtain useable data. The annular imploding plasma is visible from the fringe distortions departing from the uniformly spaced reference fringe pattern. Analysis of this data is shown in the false color image of Fig. 8. The sheath thickness was approximately 2 mm and the peak density was $1.4 \times 10^{18}\,\mathrm{cm}^{-3}$. The MRT wavelength was about 5 mm. Successive images can give an implosion velocity and can show the development of the MRT.

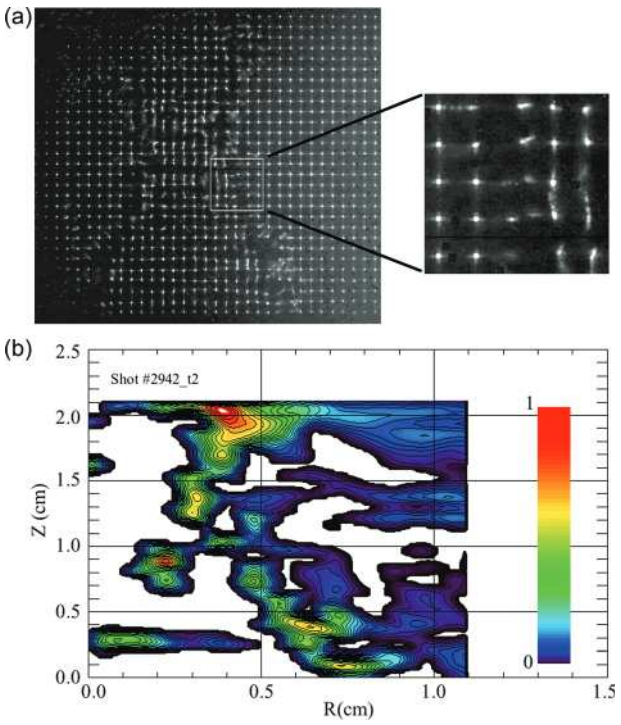

FIG. 7. Raw LWA data (a) and the derived imploded plasma density profile (b) for COBRA pulse #2942. The peak plasma density is $1.7 \times 10^{18}\,\mathrm{cm}^{-3}$. The plasma diameter was about 0.5 mm at a z = 1 cm location. The MRT wavelengths were about 4 mm. The image was taken late in time, approximately at the peak current of the solid line pulse in Fig. 1.

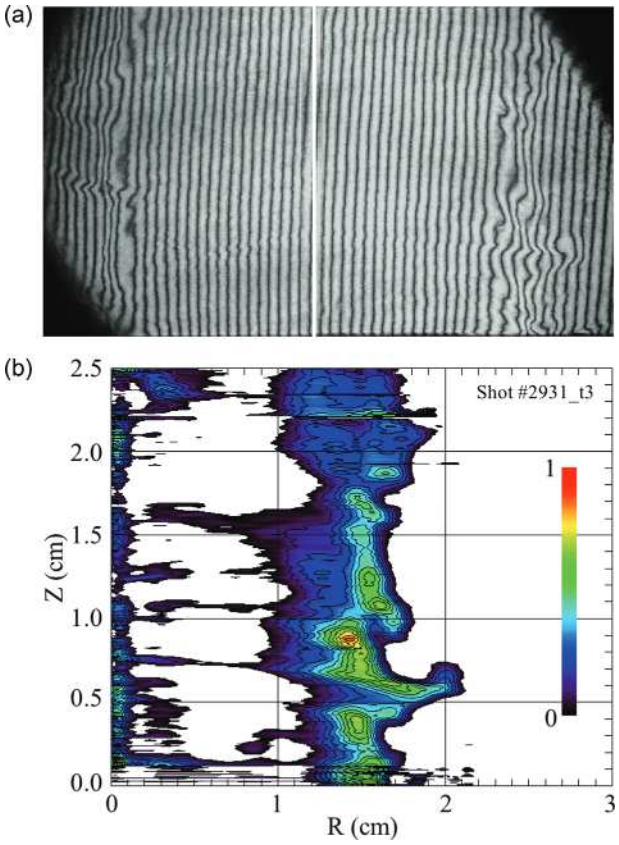

FIG. 8. (a): LSI data of an imploding gas-puff with Ne in the outer shell and Ar in the inner shell. The vertical white colored line in the middle indicates the pinch axis; (b): Measured density profile from the LSI image shown in (a).

3. Planar laser induced fluorescence

The gas-puff neutral density distributions can be measured with the laser interferometry[23–25] or PLIF. Laser interferometry is difficult at our neutral densities ($\sim 10^{16}\,\mathrm{cm}^{-3}$) and so we used the PLIF method in a separate vacuum chamber. The gas (Ne or Ar) was mixed with 5% acetone by pressure. A line focused, 10-ns, frequency-quadruped Nd:YAG laser beam passed through the diameter of the gas-puff. Fluorescence was induced in the acetone tracer and imaged using a gated, two-stage intensified CCD camera. Figure 9 shows the image of the nozzles (lower part) and the captured laser induced fluorescence (upper part). The measurements were calibrated by observing the fluorescence from a known static fill of the vacuum chamber with the same gas-acetone mixture. A detailed description of these procedures was reported in Ref. 14.

Figure 10 shows the derived R-z density profile of an Ar gas-puff. The pressures in the outer and inner nozzle

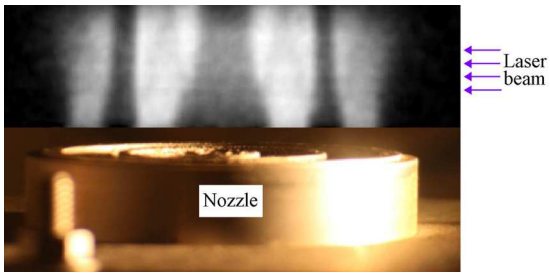

FIG. 9. Fluorescence (upper part) from an acetone-seeded Ar gas-puff.

plena were 54 and 162 Torr, respectively. The gas-puffs from the two nozzles were shell like. The peak gas density was about 10^{16} cm^{-3}. The initial density profile is not likely to be perfectly smooth spatially. The perturbations will serve as a seed for the early MRT instability. The large-scale tailoring of the density profile will then determine whether the ultimate growth of the MRT instability can be mitigated through the actual density profile during the acceleration (growth of the MRT instability on the outer surface) and deceleration (suppression of the MRT instability) phases in implosions.

III. IMPLOSION STABILITY STUDIES

For the experiments described in this section, various configurations of Ne and Ar were used in the two plena. Implosions with Ne in the outer plenum and Ar in the inner are referred to as Ne-on-Ar, etc. In all cases, the plenum pressures were adjusted to maintain, to the extent possible, the same radial mass density profile in order to focus on the stability effects of changing the gas combination. Figure 11 shows the PLIF results for an acetone seeded Ar-on-Ar puff. The Ar particle density curve (solid line) is a direct result of the PLIF measurement. The Ar mass line density curve (dashed line) is obtained by introducing the atomic weight of the gas to the PLIF data, multiplying by 2π and integrating from R to infinity. The integrated line mass density in the inner (or outer) puff is about 4 (or 6) μg/cm. Therefore, the integrated mass ratio of the inner to the outer puff is 2:3.

In this section, several experimental results will be presented. Until we were confident of the pre-ionization process, most experiments were performed with a 12.5 μm diameter Al wire on or near the axis. First, the stability properties of puff-on-puff, Ne and Ar implosions are shown. This is followed by demonstrating the effects of the 12.5 μm diameter Al wire on and slightly off axis. Next, the stability effects of using different current profiles are described. Finally, visible and X-ray spectrometry observations are presented.

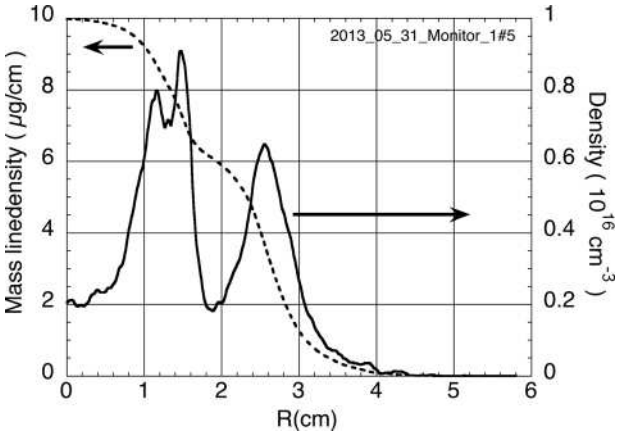

FIG. 11. Solid line is the neutral Ar particle density per unit volume of an Ar gas-puff according to the PLIF measurement. The dashed line is the Ar mass line density obtained as described in the main text. The plenum pressure ratio of the inner and outer puff valves is 3:1, which implies a mass ratio of 2:3 for the inner and outer gas-puffs.

A. Implosions with various Ne and Ar configurations

Figure 12 shows the implosion current pulse (thick black line), the X-ray signal (thin black line), and the timings of the two gated XUV cameras (short vertical lines) for COBRA pulse #2779. This was a Ne-on-Ar test. The pressures in the outer and inner plena were 108 Torr Ne and 162 Torr Ar, respectively. There were two peaks in the current waveform with the second peak higher than the first. The current reached the first peak of 0.75 MA in 80-ns, it decreased to 0.65 MA in 40 ns, and then reached the second peak of 0.9 MA at 210 ns. The current pulse was initiated 450 μs after the gas-puff injection. Peak X-ray emission (pinch time) occurred 185-ns after the current initiation. Figure 13 shows seven gated 2-ns XUV pinhole images, which captured the structure of the imploding plasma. As can be obtained from the images, the implosion velocity during the interval imaged was 20–30 cm/μs within 30 ns before the peak X-ray emission. The MRT instabilities grew slowly and their amplitudes were only 1-mm or less, resulting in a fairly uniform pinched plasma column at t = −5 ns for this 2:3 inner/outer mass ratio implosion.

The diameter of the pinched plasma was 2-mm as derived from the XUV images. It was larger at the cathode than at the anode. This zippering was due to the relative lower downstream mass density (at the anode) versus at the cathode. In later experiments, this zippering was removed by initiating the current pulse 500 μs rather than 450 μs after the start of gas-puff injection.

A filtered, time integrated four-pinhole X-ray camera was used to image the pinched plasma. The X-ray

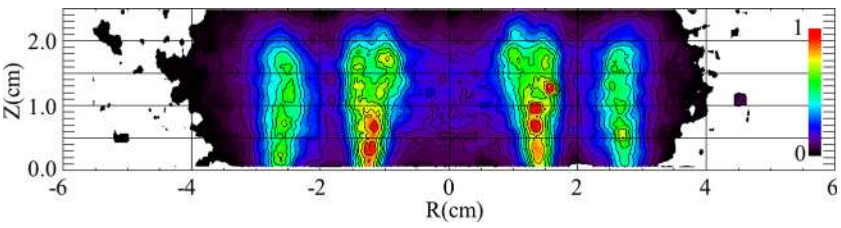

FIG. 10. The derived density profile of a double-shell Ar gas-puff. The inner and outer nozzle plena pressures were 162 and 54 Torr, respectively. The peak density was 10^{16} cm^{-3} and the area integrated line density was about 10 μg/cm.

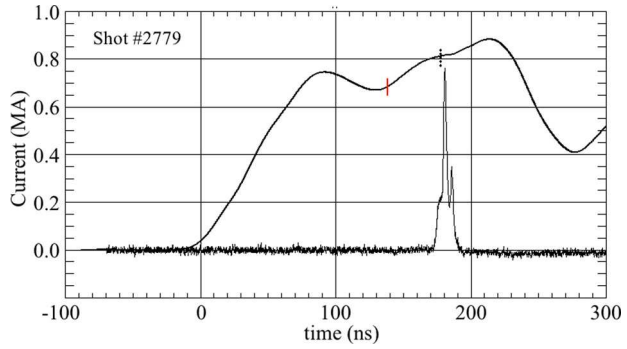

FIG. 12. Implosion current (thicker black line) and X-ray (thin black line) pulse. The vertical bar (dotted line) at t = 137 ns (178 ns) is the start of the first (or the second) 2-ns gated 4-frame XUV images, three from the first camera and four from the second.

transmissions of the various camera filters are shown in Fig. 14. Figure 15 shows the pinhole images with these filters, i.e., a 12 μm thick Be foil for X-ray photon energy E > 0.9 keV, a 200 μm Be foil for E > 2 keV, a 25 μm Al foil for 1.4 < E < 1.6 keV and E > 4 keV, and a 12.5 μm Ti foil for 2.5 < E < 4.85 keV. The X-ray radiation was distributed along the pinch axis, with clear small amplitude oscillations in radius along the entire plasma column. These correspond to the MRT instabilities and have a wavelength of about 4 mm. As shown in Fig. 15, the Ne K-shell X-ray radiation, in the image filtered by 12.5 μm Be, is ~3-mm in mean diameter with an MRT amplitude of 1-mm, while in the image filtered by the 200 μm Be foil, the Ar K-shell emission is about 2.5-mm in diameter with a peak/valley MRT amplitude of 0.6 mm. This is consistent with the gated XUV images. The pinch plasma is more or less uniform with small MRT amplitude, implying that the implosion was relatively stable.

We also studied implosions with Ne-on-Ne and Ar-on-Ne loads. Again, we adjusted the plenum pressures of the outer and inner nozzles so that the 2:3 mass ratio of the inner/outer puff and 10 μg/cm mass line density were not changed from the Ne-on-Ar case. Figure 16 shows the gated XUV images of the imploding plasma with an outer Ar (plenum pressure 54 Torr) puff on an inner Ne (324 Torr) and a Ne (108 Torr)-on-Ne(324 Torr) load. The amplitude of the MRT instability grew with time and was on the order of 5-mm from 10 ns before peak x-ray emission to the time of peak x-ray emission. There was a kink instability in the Ne-on-Ne implosion. The pinched plasma diameters were relatively large and not uniform axially as the MRT instabilities distorted the implosion and affected the compression of the plasma. The X-ray emission was weak. These implosions were less stable than the Ne-on-Ar case.

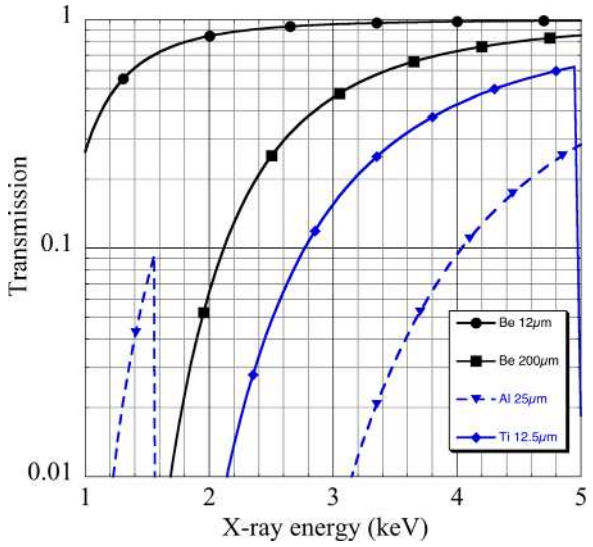

FIG. 14. Filter transmissions of the X-ray pinhole camera filter materials.

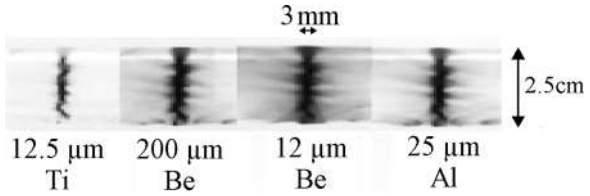

FIG. 15. Time integrated multi-pinhole images of the pinched plasma column from COBRA pulse #2779 filtered by 25 μm Al foil (1.4 < E < 1.6 keV and E > 4 keV), 12 μm Be foil (E > 0.9 keV), 200 μm Be foil (E > 2 keV), and 12.5 μm Ti Foil (2.5 < E < 4.85 keV). The radial scale is enlarged by a factor of 2 relative to the z-axial scale.

Implosions other than Ne-on-Ar showing less stability than Ne-on-Ar could be a result of the 2:3 (inner puff to outer puff) mass ratio, which may not be optimum for stability. However, that ratio was used in other high current, >200-ns implosion Z-pinches, which produced Ar K-shell x-ray yields comparable to 100-ns Z-pinches.[9,10] Optimization of the gas-puff mass density profile for stable implosions will be conducted in future experiments. Here, we have shown that besides tailoring the density profile to mitigate the MRT instability growth, tighter pinch plasmas can also produced with the choice of gas species in the two nozzles.

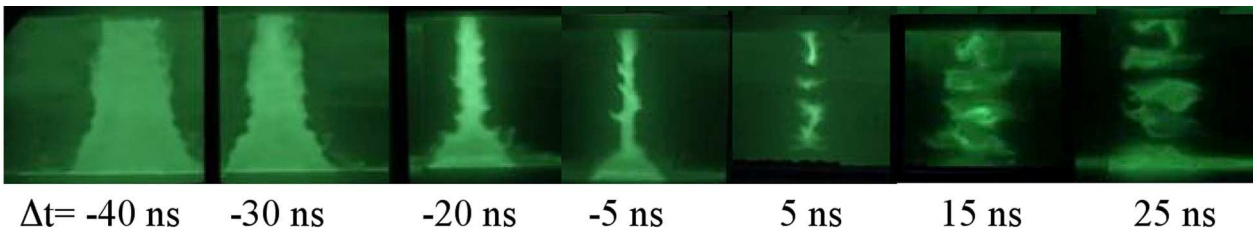

FIG. 13. Two-ns gated XUV pinhole images of the Ne-on-Ar imploding plasma without a wire on the pinch axis. The diameter of the pinholes is 200 μm. The time is relative to the peak of the X-ray emission. The anode is at the top and the cathode (high voltage side) at the bottom. The pinched plasma length is 2.5-cm. The derived pinch plasma diameter (at −5 ns) is 2-mm. (COBRA pulse # 2779).

Relatively stable implosions, which produced tighter pinch plasma, with the Ne-on-Ar load were observed in pulses other than the ones shown in figures here. One explanation could be that the implosion dynamics of Ne-on-Ar are different than the Ar-on-Ne even though the initial mass density profiles were similar. Figures 17–19 show the time evolution of the imploding plasma radius (solid line) and velocity (dashed line) at the middle of the z-axis for these pulses. The solid and open dots are plasma radius and velocity measured from the 2-ns gated XUV images, respectively. They are fitted by polynomial functions. For Ne-on-Ar loads, the peak implosion velocity was 5 cm/μs. The imploding plasmas were starting to decelerate 25-ns before the peak x-ray emission. The growth of the MRT instability was suppressed. The amplitudes of the MRT instability were 1-mm or less. A tighter, more axially uniform pinched plasma was produced. For Ar-on-Ne loads, the peak implosion velocity was over 40 cm/μs. The deceleration of the plasma occurred 10-ns before the peak of x-ray emission. For Ne-on-Ne loads, plasmas were continuously accelerated to over 40 cm/μs. In both Ar-on-Ne and Ne-on-Ne cases, the growth of the MRT instability was observed from the gated XUV images. The amplitudes of the MRT instability were 5-mm or more. These two loads gave relatively unstable implosions.

As we attempted to keep identical initial mass density profiles in the above three loads, the same by adjusting the nozzle plenum pressures, it was not expected that the implosion dynamics would be so different. For noble gases of Ar and Ne, the mass density profiles produced from a given nozzle are identical, if one keeps the plenum pressure for argon at half of that for neon. However, for the two concentric annular gas puffs, there are collisional interactions between the two shells. Reference 14 has shown that the two gas shells do not simply merge or overlap with each other, but reflected off of each other in the interface region. Such Ar-Ne collisions could result in different mass density profiles between Ne-on-Ar and Ar-on-Ne situation. If this is the case, adjusting the pressures in the nozzle plena could possibly produce a stable Ar-on-Ne implosion.

Another explanation of why Ne-on-Ar loads are relatively stable compared to the Ar-on-Ne ones could be the differences in the plasma density profiles and plasma radiation.

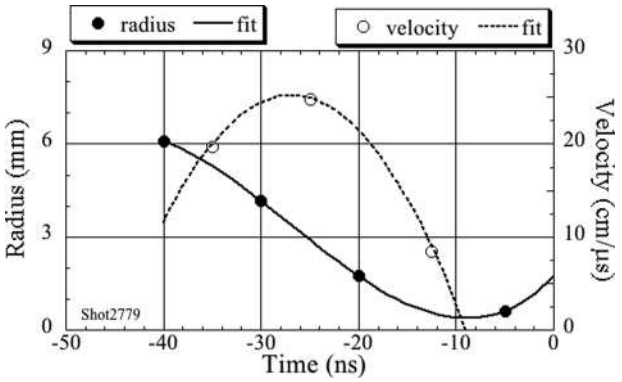

FIG. 17. Imploding plasma radius (solid line) and velocity (dashed line) vs. time with a Ne-on-Ar load, Shot #2779. The solid and open circles are the data measured from the gated XUV images, which are fitted by polynomial functions. Deceleration of the implosion occurred 25-ns before the peak x-ray emission (t = 0).

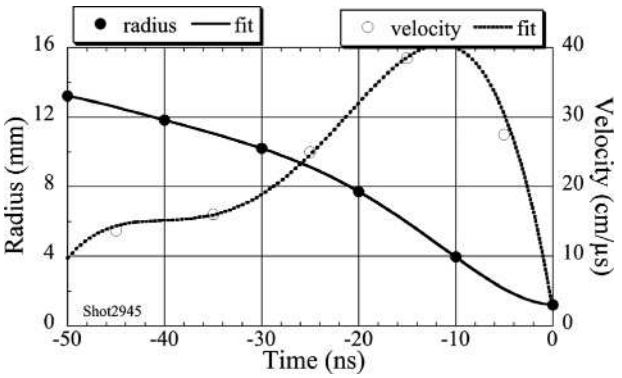

FIG. 18. Imploding plasma radius (solid line) and velocity (dashed line) vs. time with a Ar-on-Ne load, Shot #2945. The solid and open circles are the data measured from the 2-ns gated XUV images, which are fitted by polynomial functions. Deceleration of the implosion occurred 10-ns before the peak x-ray emission (t = 0).

There is a factor of four changes in the initial density profile when switching from the Ne-on-Ar to the Ar-on-Ne load. Recall that the outer gas puff has 60% of the total mass and the inner 40%. If we assume that in the pinch phase, most of the argon ions are in the He-like ionization stage and the neon ions are in the H-like state, the electron density in the

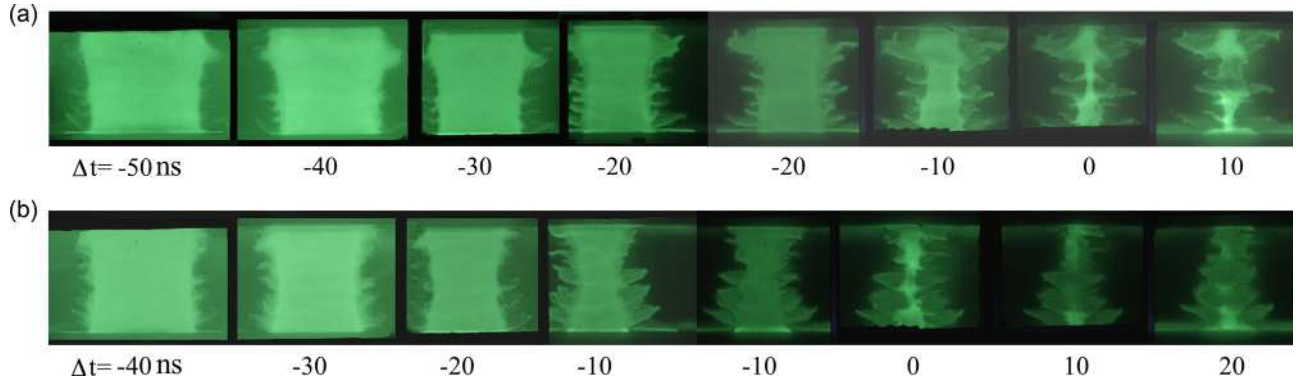

FIG. 16. Images of the imploding plasmas captured by the two 4-frame 2-ns gated XUV cameras, where the timing of the last frame in the first camera was overlapped with the first frame in the second (orthogonal view) camera at −10-ns. (a): the Ar-on-Ne (pulse # 2945); (b): Ne-on-Ne (pulse 2948). The plasma length was 2.5-cm. The time is relative to the peak of the X-ray emission. The MRT instability amplitude continuously grew in both cases.

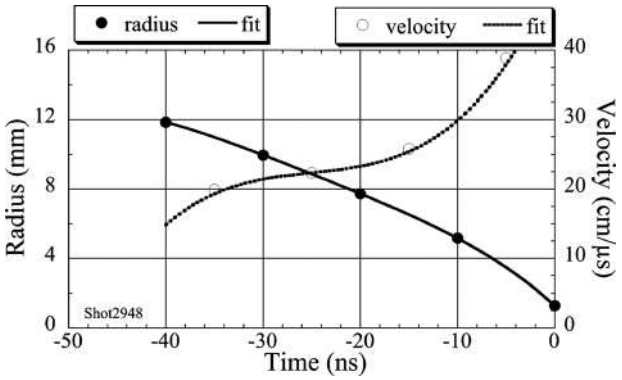

FIG. 19. Imploding plasma radius (solid line) and velocity (dashed line) vs. time with a Ne-on-Ne load, Shot #2948. The solid and open circles are the data measured from the 2-ns gated XUV images, which are fitted by polynomial functions. The imploding plasma was continuously accelerated to the pinch phase resulting in an unstable pinch plasma.

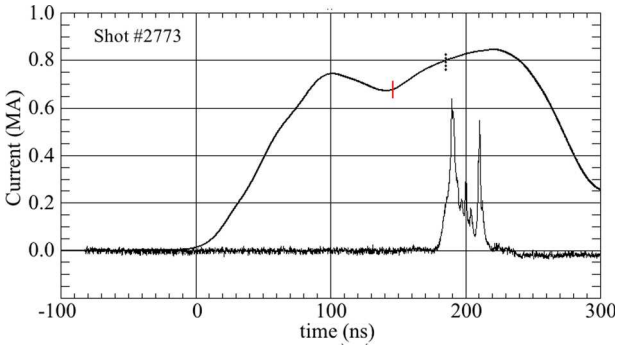

FIG. 20. Implosion current (thicker black line) and X-ray (thin black line) pulse. The vertical lines on the current pulse indicate the start of the first and second 2-ns gated 4-frame XUV images, respectively.

Ne-on-Ar case could be 20% higher than the Ar-on-Ne case. The higher-Z element, argon, plasma will radiate more energy than a low-Z, neon, plasma. For a given input energy at a >1-MA implosion current level, an argon dominated pinch plasma could be cooler than the neon dominated plasma. When the plasma pressure is comparable to the $j \times B$ compression force, the implosion dynamics will be affected and no longer be the same in the three loads, we have tested. As shown later in the x-ray spectra, the pinch plasma with an inner neon puff was hotter than with an argon inner puff. A hotter neon pinch plasma is harder to compress than a radiation cooling argon pinch plasma. This could explain why relatively fatter neon pinch plasmas are commonly observed in >1-MA implosions, including the ones reported here.

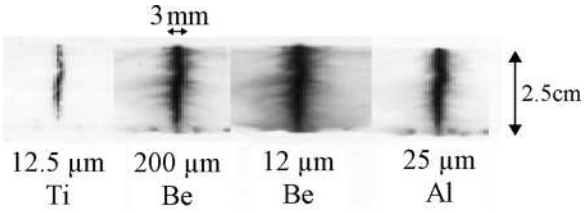

FIG. 22. Time integrated multi-pinhole images of the Ne-on-Ar pinch plasma with an Al wire on the pinch axis (pulse #2773). The filters of the pinholes were a 12 μm Be foil ($E > 900$ eV), 200 μm Be foil ($E > 2$ keV), 25 μm Al foil ($1.4 < E < 1.6$ keV and $E > 4$ keV), and 12.5 μm Ti Foil ($2.5 < E < 4.85$ keV). The radial scale is enlarged by a factor of 2 relative to the axial scale.

B. Ne/Ar implosions with a wire on the axis

Figure 20 shows the implosion current pulse (thick black line), the X-ray signal (thin black line), and the timings of the gated XUV cameras (short vertical lines) obtained from pulse #2773. This pulse was also Ne-on-Ar, but with a 12.5 μm diameter Al wire on the pinch axis. To maintain the same mass density profile, the plenum pressures were set at 108 Torr Ne and 162 Torr Ar, respectively. The current waveform was similar to the pulse without a wire (pulse #2779). There were two X-ray pulses. One is from Ne and Ar K-shell emission at 180-ns with a pulse width of 10-ns. The second was an Al and/or Ar K-shell X-ray pulse 20 ns later with a pulse width of 3-ns. Figure 21 shows eight 2-ns gated XUV images of the imploding plasma. The XUV radiation from the on-axis Al wire was observed 50-ns before the peak X-ray pulse, which is consistent with the visible plasma spectroscopy discussed later. After the first peak of the X-ray pulse, the 2-mm diameter plasma further pinched onto the Al wire and produced even tighter pinched plasma. The MRT instabilities seem damped out between the first and second X-ray peak by the on-axis mass from the ablation of the Al wire.

Figure 22 shows the time integrated X-ray images of the pinched plasma. The X-ray radiation was uniform along the pinch axis, except within 5-mm of the cathode. In this region, the X-ray radiation was weak. MRT amplitude variation along the pinched plasma column is weak. From the X-ray images, the measured source size for the X-ray radiation was 3-mm in diameter with a 12 μm Be filter (Ne K-shell), 2.5-mm with a 12 μm Al filter, 1.8-mm with a 200 μm Be filter (Ar K-shell), and 1.3-mm with a 12.5 μm Ti filter.

As a comparison, we have conducted Ar-on-Ar implosions with and without a 12.5 μm Al wire on the axis. As the mass of the Ar atom is twice that of the Ne atom, we set the

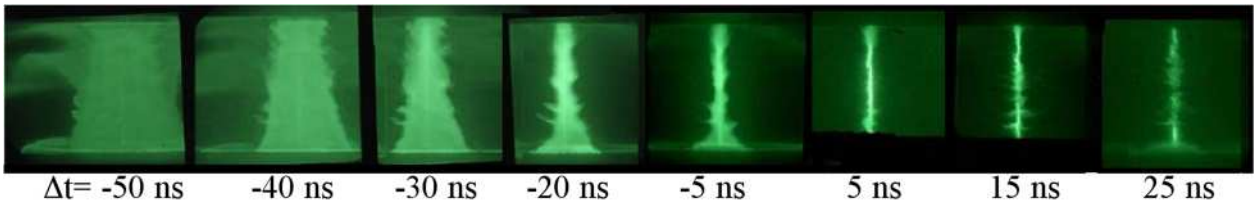

FIG. 21. Two-ns gated XUV images of the Ne-on-Ar imploding plasma with an Al wire on the pinch axis (pulse #2773). The time is relative to the first peak of the X-ray emission. The pinched plasma length is 2.5 cm and the pinched plasma diameter is 1.5-mm just before the first X-ray peak at −5 ns. It pinched down to <0.7 mm near the second X-ray peak at 15 ns.

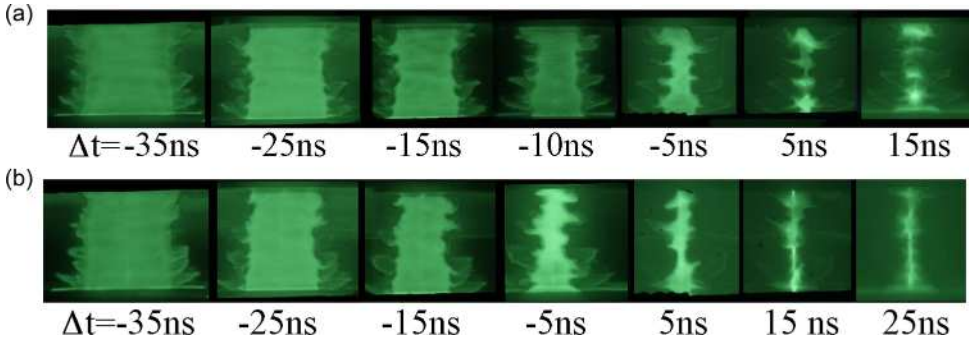

FIG. 23. Two-ns gated XUV images of the imploding plasma in Ar-on-Ar Z-pinches. (a): without a wire on the axis (pulse #2946); (b): with a 12.5 μm Al wire on the pinch axis (pulse #2934). The time is relative to the peak of the X-ray emission.

gas in the inner plenum to be 162 Torr Ar and, in the outer, it was reduced from 108 Torr Ne pressure to 54 Torr for these Ar-on Ar pulses. Thus, the mass density profile was maintained similar to the Ne-on-Ar case. Figure 23 shows the 2-ns gated XUV images with and without an on-axis Al wire. The MRT instability grew substantially and the bubbles of the MRT instability were large, which resulted in a relatively large diameter pinched plasma column. The mean diameter of the pinched plasma was 3 mm with the Al wire and 5 mm without the wire. The mass ablated from the on-axis Al wire has clearly affected the later time implosion dynamics and reduced the MRT instability amplitude in the stagnation phase. The Al pinch plasma was not axially uniform. Near the cathode ($z < 1$ cm), the MRT instability of the Ar/Ne pinched plasma has a relatively small amplitude and the Al plasma pinched down to <0.5 mm in diameter. In the other region, the pinch plasma diameter was few mm. The gated XUV image 25-ns after the x-ray peak shows that a solid core Al wire still remained intact.

The experiments suggest that the on-axis ions could be pinched down to small radius provided they were imploded by a less unstable outer plasma. We anticipate that adding a center gas jet will produce a more stable pinched plasma column.[26–28] The 12.5 μm Al wire had a mass line density of 3 μg/cm, which is comparable to the 10 μg/cm gas puff. Similar to the process in wire array Z-pinches, there was a solid Al core that did not participate in the implosion. The mass fraction of the Al wire ablated into the plasma will be estimated when the Al K-shell radiation power or energy is measured using the x-ray spectrum in future experiments.

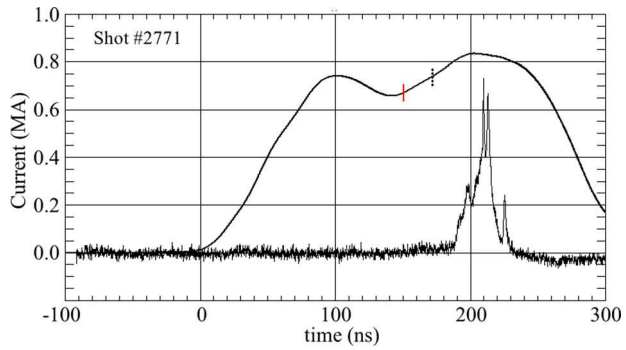

FIG. 24. Implosion current (thicker black line) and X-ray (thinner black line) pulse. The vertical lines are the start of the first or the second 2-ns gated 4-frame XUV images. Pulse #2771.

C. Ne/Ar implosions with a wire off the axis

Implosion dynamics and the interaction of the gas-puff and a solid wire were explored further by placing a 12.5 μm diameter Al wire 5-mm off the pinch axis for a Ne-on-Ar load. Figure 24 shows the implosion current pulse (thick black line), X-ray signal (thin black line), and the timing of the gated XUV cameras (short vertical lines) obtained from pulse #2771, which had the Al wire 5 mm off axis. The current waveform was typical, but the X-ray pulse was wider than with a wire on axis. Figure 25 shows the XUV images of the imploding plasma viewed from the directions parallel (upper part) and perpendicular (lower part) to the pinch-wire plane. The wire started to ablate when the puff plasma swept through it and continually ablated towards the gas-puff pinch axis. Not all of the current flowed in the puff plasma as the wire carried part of the current. The outer edge (away from the gas-puff axis) of the wire was very straight and there was no noticeable plasma expansion there. The inner edge (closer to the pinch axis) was smooth and there was ablated mass/plasma expanding towards the gas-puff pinched plasma. The wire expansion velocity was $\sim 10^7$ cm/s. Near the peak X-ray emission, two straight stagnation pinch plasma columns were produced with a separation of about 3-mm. The pinch diameter of the gas-puff was ~2 mm and the wire plasma

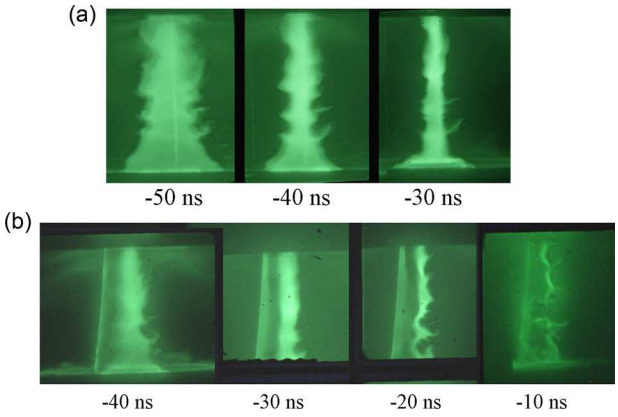

FIG. 25. Two-ns gated XUV images of the imploding plasma (pulse #2771). Upper: It was viewed parallel to the wire and gas-puff axis plane so that the wire appears to be in the center of the gas-puff; Lower: Image captured perpendicular to the wire and gas-puff axis plane. Near the peak X-ray emission, two separated plasma columns (wire and gas-puff) were observed. Time is relative to the peak of the X-ray emission. The pinch plasma length is 2.5-cm.

~0.5 mm about 30-ns before the X-ray peak. Again, the core of the Al wire did not fully vaporize during the implosion and pinch phase as there was wire mass still left at the original wire location after the pinch phase. The boundary of the wire plasma was relatively smooth without noticeable MRT bubbles, while the gas-puff plasma showed substantial structure and the instability continued to develop after the peak of the X-ray emission.

Several photo-excited x-ray lasers have been proposed, but such experiments were conducted without successes.[29–31] The main challenges in this type x-ray laser development are to produce two adjacent plasma columns with the plasma temperatures and density much higher in the photon pump source and relatively lower in the lasing medium. It might be possible that a gas puff Z-pinch with off-axis wires, as shown above, could be adapted for photo-pumped x-ray laser research. The gas-puff Z-pinches with an off-axis wire will also allow us to explore the switching and distribution of the implosion current between the puff plasma and wire.[32]

D. Current waveform effects on the implosion dynamics

In addition to the radial mass density profile and the atomic number of the gas(es), we found that the implosion dynamics was also dependent on the driving current waveform. For these experiments, two different double peaked current profiles were used as shown in Fig. 2 and in more detail in Figs. 26 and 27. The thicker black and red traces are the measured machine current and voltage, respectively. The thinner black trace is the measured dI/dt multiplied by L_0, the fixed load inductance of 12 nH. The initial neutral gas mass density profiles continued to be described by Fig. 11. The two current pulses shown in Figs. 26 and 27 drove Neon-Ar gas-puff Z-pinches with a 12.5 μm Al wire on the pinch axis. By adjusting the timing of the two Marx output switches, the amplitude of the first peak can be either lower (Case A) or higher (Case B) than the second one. Since the plasma ohmic resistance is negligible, the difference between the measured driver voltage (V) and the fixed inductive voltage is due to the inductance change associated with the radially moving plasma. We have

$$I\frac{dL}{dt} = V - L\frac{dL}{dt}, \tag{1}$$

$$L = L_0 + l\frac{\mu_0}{2\pi}ln\frac{R}{r}, \tag{2}$$

and

$$\frac{dL}{dt} = -5\times10^{-9}\frac{v_r}{r}\ \mathrm{H/s}, \tag{3}$$

where I is the current, v_r is the implosion velocity in cm/s, r (or R) is the plasma (or return current post) radius in cm, and a plasma length $l = 2.5$ cm is used. A 12 nH fixed load inductance was experimentally determined by matching the voltage monitor signal to the dI/dt pulse in the early time ($t < 100$ ns) before substantial inductance change due to the implosion. Using Eqs. (1)–(3), the measured dI/dt and the voltage values, the radius and velocity of the imploding plasma can be calculated.[33,34] In Case A (Fig. 26, pulse #2780), the IdL/dt voltage peaked at 180 kV, when the mean plasma radius was about 0.3 cm and the current was 0.8 MA. The dL/dt value was 0.225 H/s and the estimated pinch velocity was 1.3×10^7 cm/s. This condition occurred at approximately $t = 180$ ns. In Case B (Fig. 27, pulse 2778), the large voltage early in time was mostly due to $L_o\ dI/dt$. The largest IdL/dt was about 75 kV and occurred at about 170 ns when the current was about 0.75 MA and the mean plasma radius was approximately 0.3 cm. The corresponding implosion velocity was 4×10^6 cm/s. The lower IdL/dt voltage for Case B corresponds to a lower implosion velocity and reduced time integrated X-ray yield since less driver power and energy were coupled into the load. The energy, E, delivered into the Z-pinch load is given by

$$E(t) = \int_0^t I(t')\frac{d}{dt'}(LI)dt' = 0.5\int_0^t I^2(t')\frac{dL}{dt'}dt' + 0.5\int_0^t \frac{d}{dt'}(LI^2)dt', \tag{4}$$

where the first term is the kinetic energy accumulated during the implosion. Figure 28 shows the calculated kinetic energy (energy coupled to the pinch plasma). At peak X-ray emission time (t ≈ 180 ns), the kinetic energy was about 2 kJ in Case A and 1 kJ in Case B. The relative K-shell x-ray emissions were measured by filtered PCDs. Between Case A and

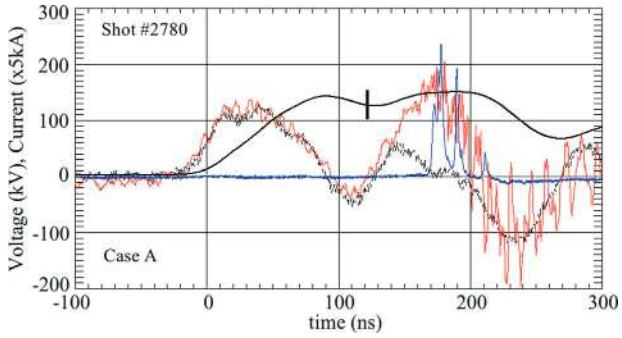

FIG. 26. Current (thick black line), $L_o\ dI/dt$ (dotted black line) voltage (red line), and X-ray (blue line, in relative unit) pulses from Pulse #2780, where the first bump of the current was lower than the second one (Case A).

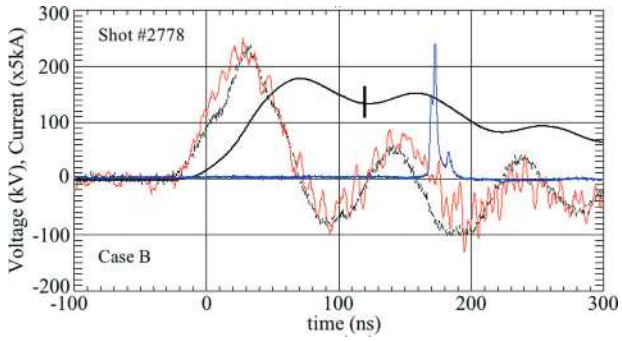

FIG. 27. Current (thick black line), $L_o\ dI/dt$ (dotted black line) voltage (red line), and X-ray (blue line, in relative unit) pulses from Pulse # 2778, where the first bump of the current was higher than the second one (Case B).

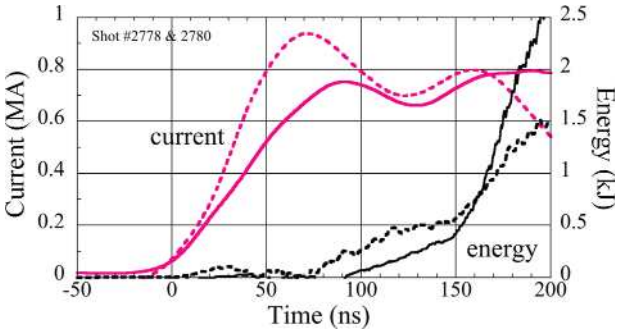

FIG. 28. Current (red color) and kinetic energy of the plasma (black color) in Cases A (dotted line) and B (solid line).

Case B, the ratios of the time integrated PCD signals were 1.6 and 1.7 with a 6 μm Mylar and 12 μm Be filter, respectively. In future, we will make precision Ar and Ne K-shell x-ray radiation power/energy measurements.

The MRT instability was also different for these two current profiles. This instability is associated with the acceleration on the outer surface during most of the implosion phase. Its growth rate will be less when the implosion acceleration is less. Figures 29 and 30 show the gated XUV images of the imploding plasma in Cases A and B, respectively. At a diameter of 0.9 cm, the plasma was decelerating as it began to stagnate in Case B, but the deceleration was less in Case A. The bubble amplitude of the MRT instability at r = 0.45 cm was smaller in Case B (stronger deceleration) than that in Case A (weaker deceleration). A tighter pinch plasma was observed in Case A than Case B as the current in Case A was higher at the pinch time. Unlike in Case A, in which plasma continuously imploded towards the axis, for Case B a 0.9 cm diameter plasma column was stagnated for over 30-ns. It then pinched on to the axis in 20-ns at a relatively lower current level.

A simple 0-D snowplow model[35] was used to calculate the imploded plasma radius and the results were compared with the XUV images. The calculated imploding plasma radius as a function of time agrees with Case A, but did not give the $\geq$30-ns plasma stagnation time observed in Case B. The snowplow model assumes that the current flows in a thin layer at the plasma edge and that the full mass in the initial gas distribution is swept inward by the radial implosion in an infinitely thin current-carrying layer. It cannot give the plasma density distribution within the sheath and does not address the current/B-field diffusion. By contrast, in the experiments, when the implosion current decreased in Case B, the magnetic field in the current sheath would quickly diffuse into the plasma as the reverse-direction current would start to flow in the outer part of the plasma, resulting in a much thicker current sheath. The reduced overall J $\times$ B leads to a reduction in the acceleration of the inner plasma implosion. The outer plasma with the reversed current density would be slowed down and perhaps even stopped by an outward J $\times$ B force. We will investigate this aspect of the implosion in the future experiments.

E. Visible light spectroscopy

The imploding plasma temperature and density can be estimated from the visible light emission spectrum. The challenge is to find suitable emission lines, from which the plasma density and temperature can be derived, such as from the emission line profiles and/or the intensity ratios of the lines. We have explored visible spectroscopy for the imploding plasmas by using one or two 19-channel, 5–10 ns gated fiber-coupled spectrometers. Figure 31 shows a simple schematic diagram of the experimental setup. A 1 $\times$ 19 optical fiber array was used to collect the chord-integrated light across the Z-pinch as shown in Fig. 31. It imaged a strip region about 0.1 mm high, 1-cm above the cathode with a radial spatial resolution of about 1 mm. The spectrometer dispersed the light in wavelength horizontally with the chordal position imaged in the vertical direction. The spectra were

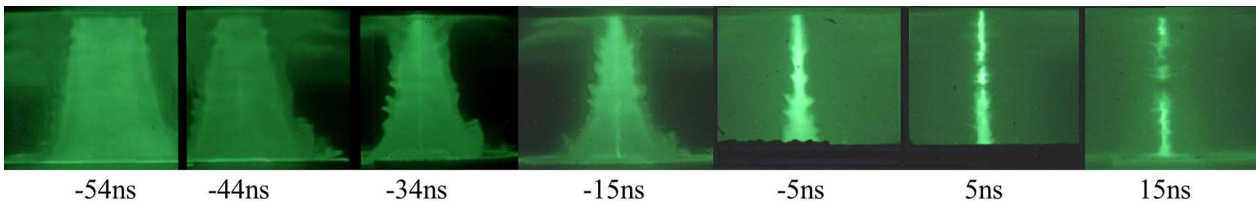

FIG. 29. Two-ns gated XUV images of the imploding plasma, where the outer Ne puff imploded on the inner Ar with a 12 μm Al wire on the pinch axis. The plasma was imploded by the current pulse shown in Fig. 23, Case A. Time is relative to the peak of the X-ray emission. (Pulse # 2480).

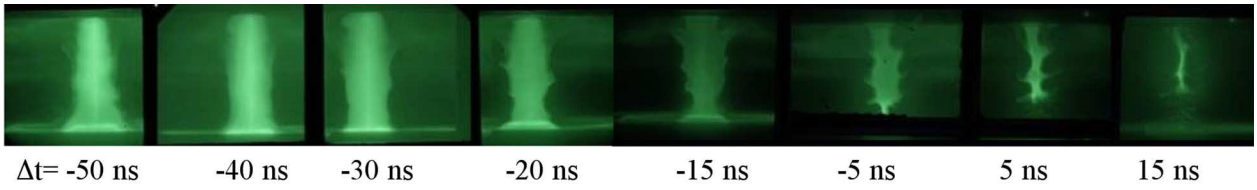

FIG. 30. Two-ns gated XUV images of the imploding plasma, where the outer Ne puff imploded on the inner Ar with a 12 μm Al wire on the pinch axis. The plasma was imploded by the current pulse shown in Fig. 23 Case B. The 0.9 cm diameter plasma stagnated for over 30 ns. Time is relative to the peak of the X-ray emission. (Pulse # 2478).

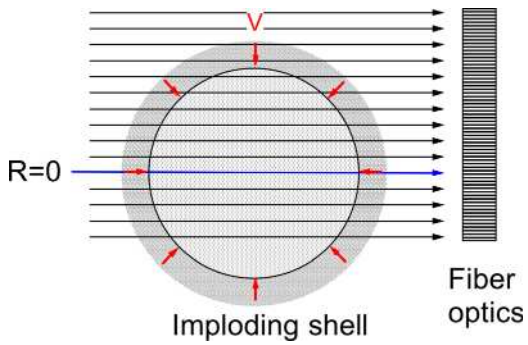

FIG. 31. Schematic diagram of the Z-pinch plasma visible light spectroscopy experimental setup.

recorded with a gated intensified charge-coupled device (ICCD).

Visible spectral lines were observable until ~30-ns before the pinch time. After that time, the plasma was too hot and the visible lines were washed out by intense continuum radiation. Figure 32 shows the plasma spectrum from

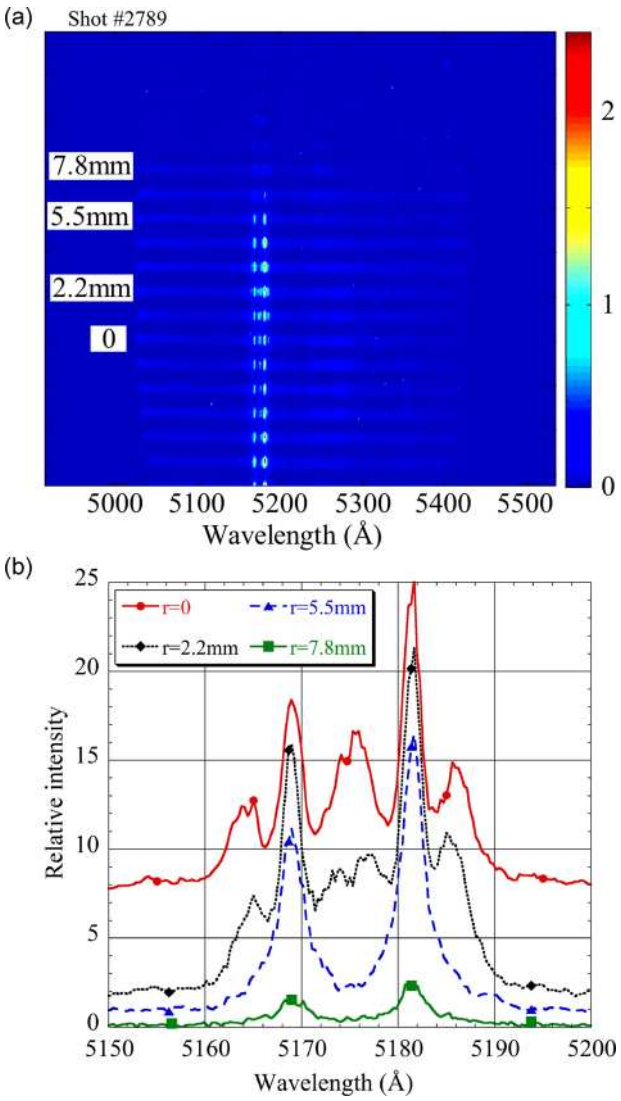

FIG. 32. (a): Chordal 5-ns gated visible spectrum of implosion plasma; (b): An expanded plot in the wavelength region 5150–5200 Å. Doppler shifts due to the imploding plasma motion are shown.

5000 to 5500 Å wavelength with a Ne-on-Ar Z-pinch. It was taken 50-ns before the peak X-ray emission. The emission fades away at a radius, $R > 8$ mm, which indicated the location of the plasma edge. That result is consistent with the gated XUV image, which indicated that the plasma edge was at $R = 9$ mm. There were several bright intensity peaks in the wavelength range of 5178 ± 15 Å. The graph in Fig. 32 is an expanded view of the spectrum at several different chordal locations. Near the edge of the plasma (7.8 mm), there were two well isolated emission lines peaked at 5169 and 5181 Å of Ar ions. Doppler shifts from the radial implosion of the plasma at this chordal position did not affect the spectral lines, but were largest at the center chord ($r = 0$). As shown in Fig. 32, due to the Doppler shift, these two emission lines (dotted blue line) were broader at $r = 5.5$ mm than those at the edge, $r = 7.8$ mm (green line). At $r = 2.2$ mm (red line), two additional peaks appeared at both the lower and higher wavelength side of each emission line. This implies that the moving plasma was annular-shell-like and at the center ($r = 0$, black line), the Doppler shifted lines were overlapped at ~5165 Å with a maximum shift of ~5 Å. This corresponds to an implosion velocity of 3×10^7 cm/s. Since the two un-shifted emission lines were also observed, this indicates that these lines were from the outer imploding plasma shell as well as from a "stationary" inner plasma. The inner plasma was very likely heated by the imploding current or shock heating because photoionization by the imploding shell plasma was insufficient to take the inner plasma to the same ionization stage as the imploding shell plasma.

The emission lines at 5169 and 5181 Å were observed in Ar or Ar/Ne Z-pinches, but not in pure Ne ones. The two lines are not found in the visible spectrum database of argon ions in various ionization stages. Most of the visible emission lines from Ar I, Ar II, and Ar III ions have been identified and calculated.[36] For Ar IV or higher charge state ions, there is very limited visible spectrum data available. In future experiments, we will attempt to determine the emitting ion charge state(s) and identify these two lines by measuring the plasma temperature and/or other means.

Figure 33 shows the visible light spectrum 90 ns before the peak X-ray emission. The load was a Ne-on-Ar configuration with a 12.5-μm diameter Al wire on the axis. The radius of the imploding plasma from this spectral image was ~10 mm. Line radiation superimposed on weak continuum radiation was observed over the whole plasma except on-axis. On the axis ($r \leq 1$ mm), there was strong continuum radiation, which was absent without an Al wire on the axis. The strong radiation also suggests that the on-axis plasma was hotter and/or more denser than the outer gas-puff plasma.

A hot on-axis plasma cannot be produced by photoionization from the cold outer plasma, but was very likely generated by current flow in the wire. In the beginning of the implosion, the gas puff was not fully ionized. Current could flow through the on-axis metal wire. An internal B_θ field could be trapped inside the imploding plasma. It has been suggested that the increased internal B_θ field that produced by the plasma compression will drive current to effectively

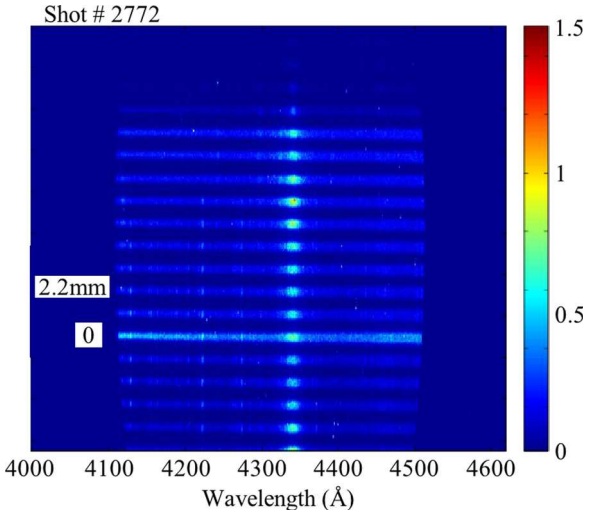

FIG. 33. Visible spectrum of implosion plasma. The intense continuum radiation at the center suggests that the on-axis plasma was hotter and/or more denser than the outer plasma.

heat the on-axis plasma.[37,38] This will be studied it in future experiments.

As shown in the experiments, the visible plasma spectra can be measured during the implosion. De-convolution of the Doppler and/or Stark broadening widths in visible emission line profiles could lead to the determination of the plasma temperature and/or density.[39]

F. Spatially resIved x-ray spectrum

The X-ray spectra of the pinched plasma were recorded using a spherical crystal spectrometer.[40,41] Mica crystals were used to capture in 1st order reflection, the ~1-keV Ne K-shell X-rays as well as in 3rd order, the ~3-keV Ar K-shell X-rays. Figure 34 shows the X-ray spectra obtained from Ne-on-Ar (lower spectrum) to Ar-on-Ne (upper spectrum) implosions. The spherical crystal allows axial resolution to be displayed vertically in the spectra shown in Fig. 34. Since the magnification of the spectral image varies for spherical crystals, the spatial resolution is not constant,

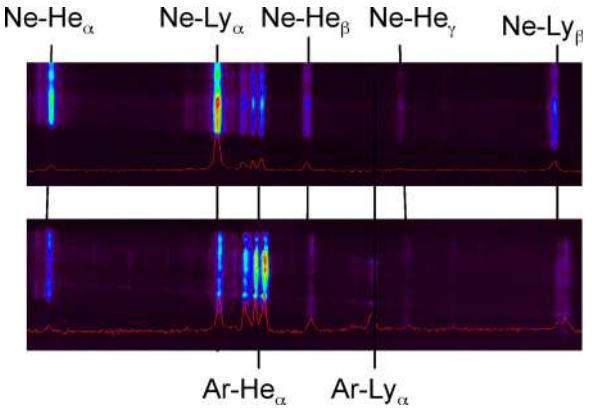

FIG. 34. X-ray spectra showing Ne and Ar K-shell radiation as a function of axial position (vertical direction). Upper: Ar-on-Ne (pulse #2942)—the Ne K-shell X-ray emission is much stronger than the Ar K-shell emission (3rd order); Lower: Ne-on-Ar (pulse #2945)—the Ar K-shell emission is much strong than the Ne K-shell emission.

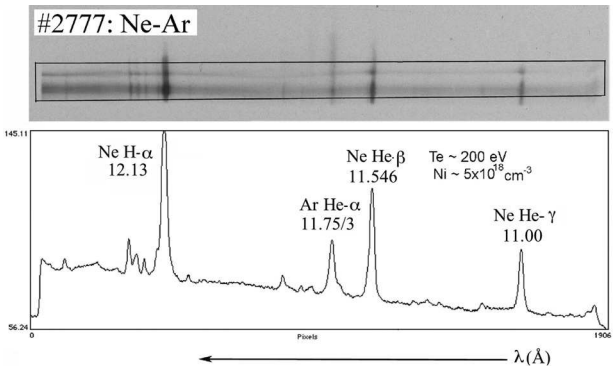

FIG. 35. K-shell X-ray spectra of Ne-on-Ar Z-pinches without a wire on the axis.

but it is in the range 100–300 μm. The spectra show Ne and Ar K-shell lines. The total energy needed to strip atoms to K-shell ionization states is much lower for Ne than that for Ar. The Ly-α (H-like, 1.022 keV) line radiation is present in the Ne K-shell spectrum, while the He-α (3.13 keV) line was dominant in the Ar K-shell spectrum. More specifically, for Ar imploding on Ne, the Ar He-α and its two satellite lines were relatively weak and the Ar Ly-α (3.32 keV) line was too weak to see. The Ne Ly-α (1.022 keV) and β (1.211 keV), He-like α (0.922 keV), β (1.074 keV), and γ (1.127 keV) lines were intense and measurable. The relative intensity ratio of the Ne and Ar K-shell emission was large. When Ar was in the inner puff, the Ar He-alpha and its satellite line radiation became intense and the Ar Ly-α line was also observed. From the X-ray emission, the ions originating in the inner puff were heated more effectively than those originating in the outer puff.

Figures 35 and 36 show the X-ray spectra in a Ne-on-Ar implosion with and without a 12.5 μm diameter Al wire on the axis, respectively. The Ne plasma density and temperature were estimated from the relative intensities of the time integrated K-shell X-rays. Comparing the X-ray spectra with and without an Al wire on the axis, the Ne plasma was denser, but cooler with the wire on the axis. More detailed spectral analysis will be reported in a separate paper.

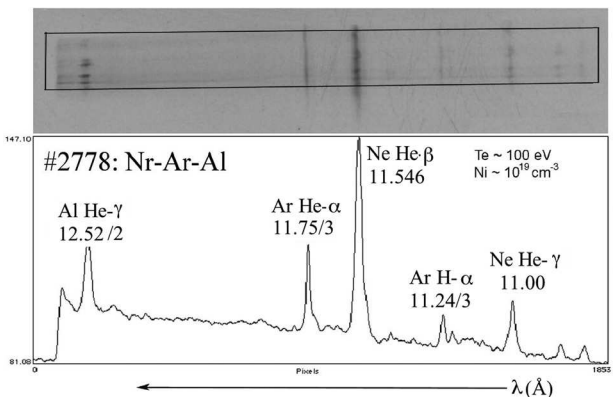

FIG. 36. K-shell X-ray spectra of Ne-on-Ar Z-pinches with a 12 μm Al wire on the axis.

IV. CONCLUSIONS AND FUTURE WORK

In summary, we have conducted double-shell gas-puff Z-pinch experiments on the 1-MA, 200-ns COBRA generator, and successfully used a set of instruments to characterize the Z-pinch implosions. Several different puff-on-puff loads with or without an on-axis Al wire have been studied. We found that Ne imploding on Ar produced a relatively stable, pinched plasma with a diameter of 2-mm. By placing an Al wire on the axis, the pinched plasma was even smaller in a diameter of 1.5 mm. Using similar radial mass density profiles, an Ar-on-Ne arrangement resulted in more unstable implosions. Gas-puff implosions with an off axis wire produced two pinched plasma columns 3 mm apart. Implosions driven by a current pulse with a higher second peak produced a 9-mm diameter stagnated plasma for over 30 ns. Visible emission lines were obtainable ~50 ns before the peak of the X-ray emission. An implosion velocity of 3×10^7 cm/s was derived from the Doppler shifts of Ar emission lines at 5169 and 5801 Å. Axially resolved Ar and Ne K-shell X-ray lines were captured using a spherical crystal spectrometer. From the X-ray spectra, we inferred estimates of the Ar and Ne plasma densities and temperatures. From the X-ray spectra, we have observed that the outer and inner plasmas were not well mixed in the pinched phase. The ions from the inner puff radiated more intense X-rays than from the outer puff. Using the LSI and LWA, we have measured implosion velocities, plasma densities, and the MRT instability wavelengths.

Future experiments for gas-puff Z-pinch studies will be conducted to investigate the issues why the Ne-on-Ar loads were relatively more stable than the Ar-on-Ne loads, and to optimize the initial gas puff mass profile for stable implosions and high x-ray yields by adding a center gas jet.

ACKNOWLEDGMENTS

We thank H. Wilhelm, T. Blanchard, and D. Hawkes for their very important support for the experiments and the COBRA facility operation. We have also benefited from many valuable discussions on gas-puff Z-pinches with Dr. John Giuliani and Dr. Alexander Velikovich of the Naval Research Laboratory, Washington DC. This research was supported by the National Nuclear Security Administration Stewardship Sciences Academic Programs under Department of Energy Cooperative Agreement No. DE-NA0001836.

[1]N. R. Pereira and J. Davis, "X-rays from Z-pinches on relativistic electron-beam generators," J. Appl. Phys. **64**, 1 (1988).
[2]D. D. Ryutov, M. S. Derzon, and M. K. Matzen, "The physics of fast Z pinches," Rev. Mod. Phys. **72**, 167 (2000).
[3]M. G. Haines, "A review of the dense Z-pinch," Plasma Phys. Controlled Fusion **53**, 093001 (2011).
[4]C. Deeney, C. A. Coverdale, and M. R. Douglas, "A review of a long implosion-time Z-pinches as efficient and high-power radiation source," Laser Part. Beams **19**, 497–506 (2001).
[5]H. Sze, P. L. Coleman, J. Banister, B. H. Failor, A. Fisher, J. S. Levine, Y. Song, E. M. Waisman, J. P. Apruzese, R. W. Clark, J. Davis, D. Mosher, J. W. Thornhill, A. L. Velikovich, B. V. Weber, C. A. Coverdale, C. Deeney, T. L. Gilliland, J. McGurn, R. B. Spielman, K. W. Struve, W. A. Stygar, and D. Bell, "Efficient Ar K-shell radiation from a Z pinch at currents >15 MA," Phys. Plasmas **8**, 3135 (2001).
[6]B. Jones, C. A. Jennings, D. C. Lamppa *et al.*, "A Renewed capability for gas-puff science on Sandia's Z machine," IEEE Trans. Plasma Sci. **43**, 1145 (2013).
[7]C. A. Coverdale, B. Jones, D. J. Ampleford, J. Chittenden, C. Jennings, J. W. Thornhill *et al.*, "K-shell X-ray sources at the Z accelerator," High Energy Density Phys. **6**, 143–152 (2010).
[8]A. L. Velikovich, F. L. Cochran, and J. Davis, "Suppression of Rayleigh-Taylor instability in Z-pinch loads with tailored density profiles," Phys. Rev. Lett. **77**, 853 (1996).
[9]H. Sze, J. Banister, B. H. Failor, J. S. Levine, N. Qi, A. L. Velikovich, J. Davis, D. Lojewski, and P. Sincerny, "Efficient radiation production in long implosion of structured gas-puff Z-pinch loads from large initial radius," Phys. Rev. Lett. **95**, 105001 (2005).
[10]R. J. Commisso, J. P. Apruzese, D. Mosher, D. P. Murphy, B. V. Weber, J. W. Banister, B. H. Failor, J. S. Levine, N. Qi, H. M. Sze, A. Bixler, P. L. Coleman, A. Jarema, L. Knight, S. Lee, M. Krishnan, J. Thompson, K. Wilson, C. A. Coverdale, and C. Deeney, "Energetics of a long-implosion-time, 12-cm-diameter Ar-gas-puff Z pinch at 6.5 MA," in *Proceedings of the 16th IEEE Pulsed Power Conference* (2007), p. 1773.
[11]P. L. Coleman, M. Krishnan, J. R. Thompson, J. W. Banister, B. H. Failor, J. S. Levine, N. Qi, H. M. Sze, J. P. Apruzese, J. Davis, J. W. Thornhill, A. L. Velikovich, R. J. Commisso, and A. Verma, "Recent results for large diameter (12 cm) gas-puff Z-pinches at peak currents of 3-6 MA," AIP Conf. Proc. **808**, 163–168 (2006).
[12]J. L. Giuliani, F. N. Beg, R. M. Gilgenbach, V. L. Kantsyrev, B. R. Kusse, V. V. Ivanov, and R. Presura, "Plasma pinch research on University pulsed-power generators in the United States," IEEE Trans. Plasma Sci. **40**, 3246–3264 (2012).
[13]P.-A. Gourdain, R. J. Concepcion, M. T. Evans, J. B. Greenly, D. A. Hammer, C. L. Hoyt, E. Kroupp, B. R. Kusse, Y. Maron, A. S. Novick, S. A. Pikuz, N. Qi, G. Rondeau, E. Rosenberg, P. C. Schrafel, C. E. Seyler, and T. C. Shelkovenko, "Initial magnetic field compression studies using gas-puff Z-pinches and thin liners on COBRA," Nucl. Fusion **53**, 083006 (2013).
[14]N. Qi, B. H. Failor, J. Banister, J. S. Levine, H. M. Sze, and D. Lojewski, "Two dimensional gas density and velocity distributions of a 12-cm-diameter, triple-nozzle Ar Z-pinch load," IEEE Trans. Plasma Sci. **33**, 752 (2005).
[15]S. L. Jackson, B. V. Weber, D. Mosher, D. G. Phipps, S. J. Stephanakis, R. J. Commisso, N. Qi, B. H. Failor, and P. L. Coleman, "A comparison of planar, laser-induced fluorescence, and high-sensitivity interferometry techniques for gas-puff nozzle density measurements," Rev. Sci. Instrum. **79**, 10E717 (2008).
[16]B. H. Failor, S. Chantrenne, P. L. Coleman, J. S. Levine, Y. Song, and H. M. Sze, "Proof-of-principle laser-induced fluorescence measurements of gas distributions from supersonic nozzles," Rev. Sci. Instrum. **74**, 1070 (2003).
[17]N. Qi, J. Schein, J. Thompson, P. Coleman, M. McFarland, R. Prasad, M. Krishnan, B. Weber, B. Moosman, J. Schumer, D. Mosher, R. Commisso, and D. Bell, "Z-pinch imploding plasma density profile measurements using a two-frame laser shearing interferometer," IEEE Trans. Plasma Sci. **30**, 227 (2002).
[18]S. A. Pikuz, V. M. Romanova, N. V. Baryshnikov, M. Hu, B. R. Kusse, D. B. Sinars, T. A. Shelkovenko, and D. A. Hammer, "A simple air wedge shearing interferometer for studying exploding wires," Rev. Sci. Instrum. **72**, 1098 (2001).
[19]N. Qi, R. R. Prasad, K. Campbell, P. Coleman, M. Krishnan, B. V. Weber, S. J. Stephanakis, and D. Mosher, "Laser wavefront analyzer for imploding plasma density and current profile measurements," Rev. Sci. Instrum. **75**, 3442 (2004).
[20]Y. Song, P. Coleman, B. H. Failor, A. Fisher, R. Ingermanson, J. S. Levine, H. Sze, E. Waisman, R. J. Commisso, T. Cochran, J. Davis, B. Moosman, A. L. Velikovich, B. V. Weber, D. Bell, and R. Schneider, "Valve and nozzle design for injecting a shell-on-shell gas-puff load into a Z pinch," Rev. Sci. Instrum. **71**, 3080 (2000).
[21]I. C. Blesener, J. B. Greenly, B. R. Kusse, K. S. Blesener, C. E. Seyler, and D. A. Hammer, "Pinching of ablation streams via magnetic field curvature in wire-array Z-pinches," Phys. Plasmas **19**, 022109 (2012).
[22]C. L. Hoyt, P. F. Knapp, S. A. Pikuz, T. A. Shelkovenko, A. D. Cahill, P.-A. Gourdain, J. B. Greenly, B. R. Kusse, and D. A. Hammer, "Cable array Z-pinch experiments at 1 MA," IEEE Trans. Plasma Sci. **40**, 3367 (2012).
[23]M. Krishnan, K. W. Elliott, R. E. Madden, P. L. Coleman, J. R. Thompson, A. Bixler *et al.*, "Architecture, implementation, and testing of a multiple-shell gas injection system for high current implosions on the Z accelerator," Rev. Sci. Instrum. **84**, 063504–1 (2013).

[24]B. V. Weber, S. J. Stephanakis, and B. Moosman, Rev. Sci. Instrum. **70**,687 (1999).
[25]P. L. Coleman, D. C. Lamppa, R. E. Madden, K. Wilson-Elliott, B. Jones, D. J. Ampleford, D. E. Bliss, C. Jennings, A. Bixler, and M. Krishnan, "Development and use of a two-dimensional interferometer to measure mass flow from a multi-shell Z-pinch gas-puff," Rev. Sci. Instrum. **83**, 083116 (2012).
[26]F. J. Wessel, P. L. Coleman, N. Loter, H. U. Rahman, J. Rauch, and J. Thompson, "Enhanced plasma radiation source: Tandem-puff, pinch-on-wire plasma," J. Appl. Phys. **81**, 3410 (1997).
[27]J. S. Levine, J. W. Banister, B. H. Failor, N. Qi, H. M. Sze, A. L. Velikovich, R. J. Commisso, J. Davis, and D. Lojewski, "Implosion dynamics and radiative characteristics of a high yield structured gas-puff load," Phys. Plasmas **13**, 082702 (2006).
[28]A. Chuvatin, L. I. Rudakov, A. L. Velikovich, J. Davis, and V. I. Oreshkin, "Heating of the on-axis plasma in long-implosion plasma radiation sources," in *Proceedings of the IEEE International Conference on Plasma Science, Baltimore, MD*, 28 June 2004, p. 361.
[29]F. C. Young, D. D. Hinshelwood, J. P. Apruzese, C. Deeney, T. Nash, and R. R. Prasad, "Implosions of NaF plasmas for photopumping a Na–Ne X-ray laser," J. Appl. Phys. **69**, 7520 (1991).
[30]N. Qi and D. A. Hammer, "Modeling the coaxial double Z-pinch for the Al XI–Mg IX laser at 228 Å," J. Appl. Phys. **74**, 4303 (1993).
[31]J. Nilsen and H. A. Scott, "Using the x-ray free-electron laser to drive a photo-pumped helium-like neon x-ray laser at 23 nm," High Energy Density Phys. **7**, 6 (2011).
[32]R. B. Baksht, A. Y. Labetsky, A. G. Rousskikh, A. V. Fedyunin, A. V. Shishlov, V. A. Kokshenev, N. E. Kurmaev, and F. I. Fursov, "Investigation of the mechanism for current switching from the outer gas-puff to the inner wire array in a structured Z-pinch," Plasma Phys. Rep. **27**, 557 (2001).
[33]D. P. Murphy, R. J. Allen, B. V. Weber, R. J. Commisso, J. P. Apruzese, D. G. Phipps, and D. Mosher, "Time-resolved voltage measurements of Z-pinch radiation sources with a vacuum voltmeter," Rev. Sci. Instrum. **79**, 10E306 (2008).
[34]G. C. Burdiak, S. V. Lebedev, G. N. Hall, A. J. Harvey-Thompson, F. Suzuki-Vidal, G. F. Swadling, E. Khoory, L. Pickworth, S. N. Bland, P. de Grouchy, and J. Skidmore, "Determination of the inductance of imploding wire array Z-pinches using measurements of load voltage," Phys. Plasmas **20**, 032705 (2013).
[35]D. Mosher, B. V. Weber, B. Moosman, R. J. Commisso, P. Coleman, E. Waisman, H. Sze, Y. Song, D. Parks, P. Steen, J. Levine, B. Failor, and A. Fisher, Laser Part. Beams **19**, 579 (2001).
[36]E. B. Saloman, "Energy levels and observed spectral lines of ionized argon, Ar II through Ar XVIII," J. Phys. Chem. Ref. Data **39**, 033101 (2010).
[37]H. U. Rahman, P. Ney, F. J. Wessel, and N. Rostoker, "Inertial confinement fusion in a Z-theta pinch," Comments Plasma Phys. Controlled Fusion **15**, 339 (1994).
[38]J. Davis, N. A. Golub, and A. L. Velikovich, Appl. Phys. Lett. **70**, 170 (1997).
[39]G. V. Vogman and U. Shumlak, "Deconvolution of stark broadened spectra for multi-point density measurements in a flow Z-pinch," Rev. Sci. Instrum. **82**, 103504 (2011).
[40]T. A. Pikuz, A. Y. Faenov, S. A. Pikuz, V. M. Romanova, and T. A. Shelkovenko, "Bragg x-ray optics for imaging spectroscopy of plasma microsources," J. X-ray Sci. Technol. **5**, 323 (1995).
[41]P. F. Knapp, S. A. Pikuz, T. A. Shelkovenko, D. A. Hammer, and S. B. Hansen, "High resolution absorption spectroscopy of exploding wire plasmas using an x-pinch X-ray source and spherically bent crystal," Rev. Sci. Instrum. **82**, 063501 (2011).